Journal of ELECTRONIC MATERIALS, Vol. 49, No. 9, 2020
https://doi.org/10.1007/s11664-020-08268-7

Recycled MnO_2 Nanoflowers and Graphene Nanosheets for Low-Cost and High Performance Asymmetric Supercapacitor

GOMAA A.M. ALI [1,2,3]

1.—Chemistry Department, Faculty of Science, Al–Azhar University, Assiut 71524, Egypt. 2.—e-mail: gomaasanad@azhar.edu.eg. 3.—e-mail: gomaasanad@gmail.com

Electrochemical materials, namely MnO_2 and reduced graphene oxide (rGO), have been prepared in diverse morphologies (nanoflowers and nanosheets, respectively). Different physical and chemical characterizations were conducted to investigate the material structure and morphology. Electrochemical properties of these materials have been studied comprehensively using cyclic voltammetry, galvanostatic charge–discharge, and electrochemical impedance spectroscopy to evaluate their suitability for supercapacitive energy storage. MnO_2 nanoflowers were obtained by recycling spent batteries. The single electrodes of MnO_2 nanoflowers and rGO nanosheets exhibit a high specific capacitance of 208.5 F g^{-1} and 145 F g^{-1}, respectively. Therefore, an asymmetrical supercapacitor was fabricated from both materials and electrochemically evaluated. It shows a superb supercapacitive performance of up to 2.0 V in Na_2SO_4. The asymmetrical supercapacitor produces a high specific capacitance (177.6 F g^{-1}), energy density (24.7 Wh kg^{-1}) and stability (95.2% over 4000 cycles). The findings recommend using MnO_2 nanoflowers and rGO nanosheets as an asymmetric supercapacitor.

Key words: Asymmetric supercapacitor, energy storage, graphene nanosheets, MnO_2 nanoflowers

INTRODUCTION

Supercapacitors are classified into two main categories based on their energy storage mechanism: pseudocapacitors (PCs) and electrochemical double-layer capacitors (EDLCs).[1–5] PCs store electrical energy faradically by electron charge transfer between the electrode and the electrolyte. The electrode materials for PCs include metal oxides, metal hydroxides, metal sulfides and conducting polymers.[6–12] In EDLCs, a double layer of electrolyte ions is formed on the surface of the electrode material. The electrode materials for EDLCs include all carbon-based materials.[13–17] Supercapacitors can be used in many applications because of their higher energy output as compared to conventional capacitors and higher power than batteries, in addition to their miniature size. Many studies have investigated different materials for supercapacitor applications with high power and long-life criteria for better energy storage devices. The morphological and structural characteristics of the electrode materials are the key factors for the energy storage properties.[18–21]

Recently, manganese dioxide (MnO_2) has drawn increasing attention as a supercapacitor electrode, as a result of its abundance and high specific capacitance (C_s) of 700 F g^{-1}.[22,23] The capacitive mechanism in MnO_2 arises from ion insertion/desertion, and therefore it depends crucially on the morphology and porosity. MnO_2 was prepared with different morphologies, such as nanoflakes,[24] nanorods,[25] nanowires,[26] nanopetals, [27] spongy-like,[28] and nanosheets.[29] Due to high Mn content

(Received March 16, 2020; accepted June 10, 2020; published online June 30, 2020)

in zinc-carbon (Zn-C) batteries, it is considered as a low-cost precursor. MnO_2 in nanoflower morphology and a mesoporous structure was successfully obtained by battery recycling, as reported in our previous works.[30,31]

On the other hand, carbon materials are extensively used in supercapacitor fabrication. Graphene, which has a high theoretical surface area, excellent electrical conductivity, and mechanical and chemical stabilities [32] is a promising candidate for energy storage applications. The charge carriers move ballistically in the 2D crystal lattice of graphene. Various chemical, electrochemical and thermal methods have been reported for the preparation of graphene.[32–34] It shows high-end capacitance values of 135 F g^{-1} in aqueous, 99 F g^{-1} in organic and 154.1 F g^{-1} in ionic electrolytes.[14,32] Graphene is an ideal EDL capacitive material due to its fascinating nanosheet structure, which makes all areas easily reachable by the electrolyte ions, and it is capable of storing a value of 550 F g^{-1}.[14]

Depending on the type of cell assembly, supercapacitors are often categorized as symmetric supercapacitors (SSCs) and asymmetric supercapacitors (ASSCs). In SSCs, two identical electrodes from the same active materials (often EDLCs materials) are used as positive and negative electrodes, while in ASSCs, two different electrodes (usually one is carbon material and the other metal oxide) are used. Thus, the hybridization of an EDLCs and Faradic pseudocapacitive systems could be a good candidate for a supercapacitor with high capacitance and energy.[35] Symmetric (NiO/NiO) and asymmetric (NiO/activated carbon) supercapacitors have shown that the asymmetric configuration has a higher C_s and higher relaxation time constant.[36,37] Asymmetric MWCNT-NiO/MWCNT in a H_2SO_4 solution showed a very high C_s of 950 F g^{-1} compared to symmetric MWCNT-NiO/NiO-MWCNT, which only showed 80 F g^{-1}.[38]

In this study, asymmetric supercapacitor-based low-cost electrodes from MnO_2 (recovered from a Zn-C battery) and reduced graphene oxide (rGO) were fabricated and evaluated. Detailed electrochemical tests were conducted on single electrodes and the full cell to evaluate their supercapacitive behaviour.

EXPERIMENTAL TECHNIQUES

Samples Preparation

MnO_2 nanoflowers (MnO_2-NF) were obtained by recycling a spent Zn-C battery (EVEREADY® D cell) using a leaching process followed by electrodeposition, as reported in our previous work.[31] Briefly, the Zn-C battery cathode powder was dried, ground, sieved to below 200 μm in size, washed with deionized water, and subsequently dissolved in H_2SO_4 and $H_2C_2O_4$. Then, using an applied current on two identical stainless-steel electrodes, the manganese oxide was precipitated as a dark powder. The graphene oxide was obtained from graphite by Hummers' method [39] and then reduced into reduced graphene oxide nanosheets (rGONS), as reported in our previous publication.[40] The prepared materials are fully characterized, and the data (including XRD, SEM/EDS, TEM, FTIR, UV–vis, Raman) are provided in our previous works.[31,40] The current study focuses on the supercapacitance performance of the practical asymmetric supercapacitor evaluated from both materials as anode and cathode.

Supercapacitance Performance

The electrochemical characterizations were performed on the electrodes prepared from MnO_2 or rGONS as an active material blended with carbon black and polyvinylidene fluoride in the weight ratio of 90:5:5 on nickel foam. Then, the electrode was pressed at 5 tons, and the mass of the active material was determined by a Shimadzu AUW220D, Japan, microbalance.

Two cell designs were used for the supercapacitive testing: a three-electrode system (3ES) and a two-electrode system (2ES). The 3ES consisted of the active material, Ag/AgCl and Pt wire as working, reference and counter electrodes, respectively. In the 2ES, a coin cell design was fabricated using two working electrodes separated by a porous membrane.

An AUTOLAB PGSTAT30 electrochemical workstation was used for the electrochemical data collection. Cyclic voltammetry (CV) and galvanostatic charge–discharge (CDC) experiments were conducted at different scan rates and different current densities, respectively, under different potential ranges. Electrochemical impedance spectroscopy (EIS) data were obtained at open circuit potential with an a.c. amplitude of 10 mV in the frequency range from 50 kHz to 0.01 Hz. The electrochemical measurements were performed in 1 M Na_2SO_4.

The C_s was calculated from CDC curves according to Eq. 1,[41–43]:

$$C_s = \frac{I}{m(\Delta V/\Delta t_d)} \tag{1}$$

where I, m, ΔV and Δt_d are the current, active material mass, potential window and discharge time, respectively.[42,44,45]

Based on the capacitance values of the positive and negative electrodes (MnO_2 and rGONS, respectively), the charge balance of the asymmetric device was optimized $Q^+ = Q^-$[42,46]:

$$\frac{m^+}{m^-} = \frac{C_s^- \Delta V^-}{C_s^+ \Delta V^+} \tag{2}$$

The energy (E) and power (P) densities were obtained from the CDC data using Eqs. 3 and 4, respectively:[42,47]

$$E = \frac{1}{2} C_s V^2 \quad (3)$$

$$P = \frac{E}{\Delta t_d} \quad (4)$$

The Coulombic efficiency (η) can be calculated using Eq. 5[41,42]:

$$\eta = \frac{\Delta t_d}{\Delta t_c}(100\%) \quad (5)$$

where Δt_c is the charge time.

Moreover, the electrochemical active specific surface area can be obtained by Eq. 6[30]:

$$S_E = \frac{C_{dl}}{C_d} \quad (6)$$

where C_d is a constant (20 and 60 μF cm^{-2} for the carbon and metal oxide materials, respectively),[34,40,48–50] C_{dl} was obtained from the impedance data at 0.01 Hz as ($C_{dl} = 1/(2\pi f m Z'')$, where, f is the frequency and Z'' is the imaginary part of the impedance.

RESULTS AND DISCUSSION

Constitutional and Morphological Studies

Recovered MnO_2-NF shows a birnessite phase and nanoflower morphology. Detailed information on the structural and morphological characteristics was reported in our previous work.[31] In addition, rGONS was fully characterized by different techniques, including x-ray diffraction, FTIR, thermal analyses, Raman spectroscopy, and FESEM to elucidate its properties. Nanosheet morphology and mesoporous structure with a specific surface area of 124.1 m^2 g^{-1} were the main findings of rGONS.[40]

Electrochemical Properties

As mentioned in the electrode preparation section, the active materials were pasted on Ni foam. Ni foam acts as a current collector as well as providing a highly accessible surface area for loading materials with a 3D porous network structure. To determine the bare Ni foam contribution to the specific capacitance, the bare Ni foam was tested by the CV and CDC under the same experimental conditions. Supplementary Fig. S1(a, b) shows the representative CV curves for the bare Ni foam substrate electrode at different scan rates in 1 M Na_2SO_4 under different potential ranges of (0–1) V and (– 1–0) V, respectively. The CV curves of the bare Ni substrate show a very narrow area and small current ,indicating a minimal specific capacitance contribution; therefore, it can be neglected. In addition, the Ni foam substrate shows a very short discharge time of less than 1 s at 0.5 A g^{-1} which gives the values 0.30 F g^{-1} and 0.25 F g^{-1} for (0–1) V and (– 1–0) V, respectively (see Supplementary Fig. S1c). The low value of contribution here may be due to the uniaxially pressing (5 tons) of the Ni foam into a thin sheet which will reduce its porosity. Similar findings of the Ni foam contribution have been reported by other authors.[30,51] Therefore, the contribution of the Ni foam substrate in the electrochemical performance and parameters can be neglected.

Supercapacitor Electrodes Performance

The CV within a potential window from 0 V to 1 V in 1 M Na_2SO_4 electrolyte was conducted to evaluate the MnO_2 electrode charge storage properties. In CV, MnO_2 nanoflowers exhibit an almost rectangular shape (Fig. 1a) at various scan rates, indicating a good charge propagation. This is a result of the 3D nanoflower morphology facilitating ion diffusion within the structure. The galvanostatic CDC curve of the MnO_2 electrode is displayed in Fig. 1(b). It can be seen that the CDC curves are linear and symmetrical with insignificant iR drop at different current densities. The C_s is calculated from the slope of the discharge curve, as shown in Fig. 1(c). MnO_2 shows high C_s even at high discharge current densities (208.5 F g^{-1} and 174 F g^{-1}, respectively, at 0.1 and 5.0 A g^{-1}). These findings are higher than those reported for MnO_2 prepared by potentiostatic and galvanostatic modes from $MnSO_4$ (237, 196 and 184 F g^{-1}, respectively, at 2 mA) [52] and for MnO_2 hollow structures (169 and 111 F g^{-1} at 0.25 A g^{-1}).[53]

In addition, in the case of acidic electrolytes (HCl), the H_2 evolution due to H^+ reduction takes place at – 0.2 V, which limits the potential window to 1.2 V. On the other hand, in basic electrolytes (KOH), the O_2 evolution due to OH^- oxidation takes place at 0.7 V which limits the potential window to 1.8 V. In the case of neutral electrolytes (Na_2SO_4), the current due to H^+ reduction and OH^- oxidation is very low; therefore, no gas evaluation reactions occur.[54] To verify the potential limits, CV was performed between different voltage windows, as shown in Fig. 2(a) at 25 mV s^{-1}. The CV curve is a clear rectangular shape in the potential range from – 1 V to 0 V (for rGONS) and from 0 V to 1 V (for MnO_2) and symmetrical around zero without the Faradaic redox peaks. In addition, CDC curves for both MnO_2 and rGONS are shown in Fig. 2(b), displaying the linear curves. The same feature is observed at all scan rates, as shown in Fig. 3(a, b). Coulombic efficiency was calculated from the CV curves of the system under different operating voltage windows. Coulombic efficiency was found to be 99.7 and 96.5% in the voltage ranges (– 1–0) and (0–1), respectively. Therefore, further electrochemical tests for rGONS have been conducted in the range of – 1–0 V. On the other hand, Fig. 3(c, d) shows the CDC curves for rGONS at different

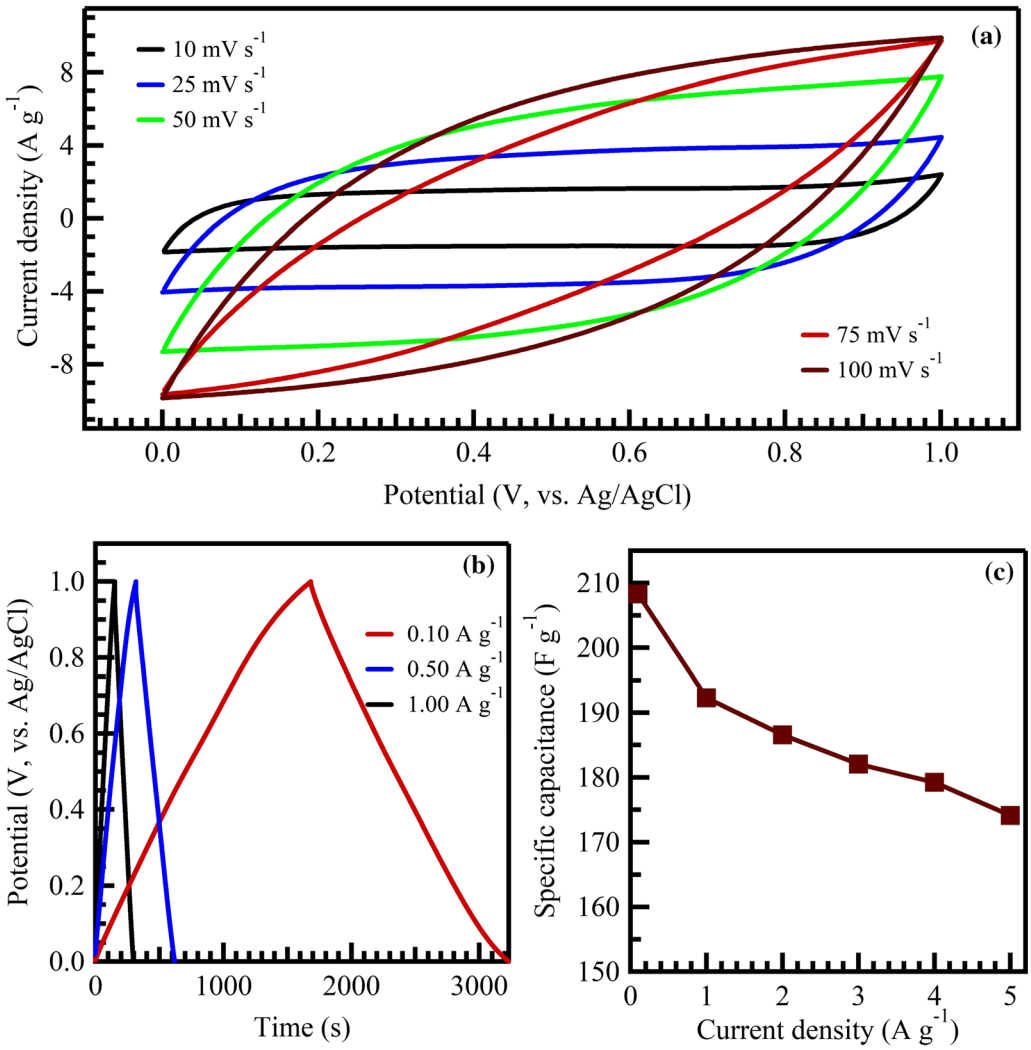

Fig. 1. Cyclic voltammograms at different scan rates (a), galvanostatic charge–discharge curves under different current densities (b), and the specific capacitance dependence on current density (c) for MnO_2-NF in 1 M Na_2SO_4.

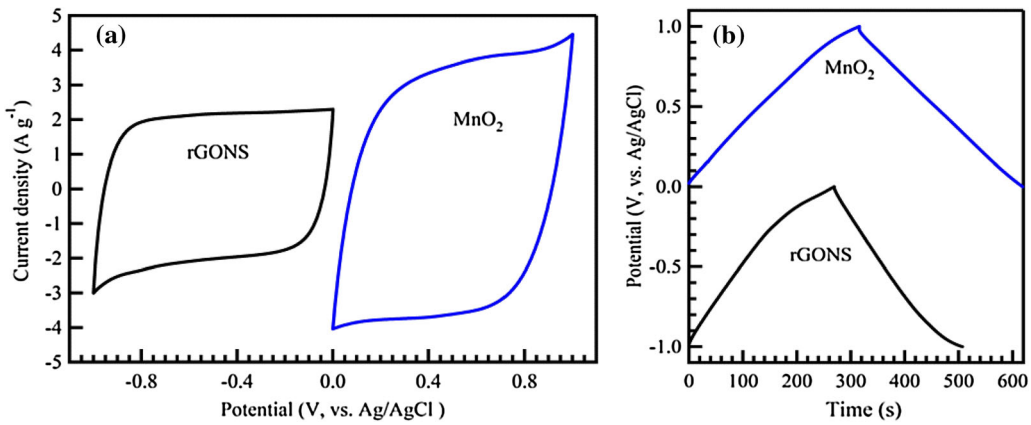

Fig. 2. Cyclic voltammograms at 25 mV s^{-1} (a) and galvanostatic charge–discharge curves (b) under different potential windows for rGONS in 1 M Na_2SO_4.

current densities in the ranges from – 1 V to 0 V and 0 V to 1 V. Linear CDC curves with in ignored iR drop are observed, indicating that the electrodes have a low resistance which leads to better EDL performance. The specific capacitance of the rGONS electrode was plotted, as shown in Fig. 3(e). The C_s

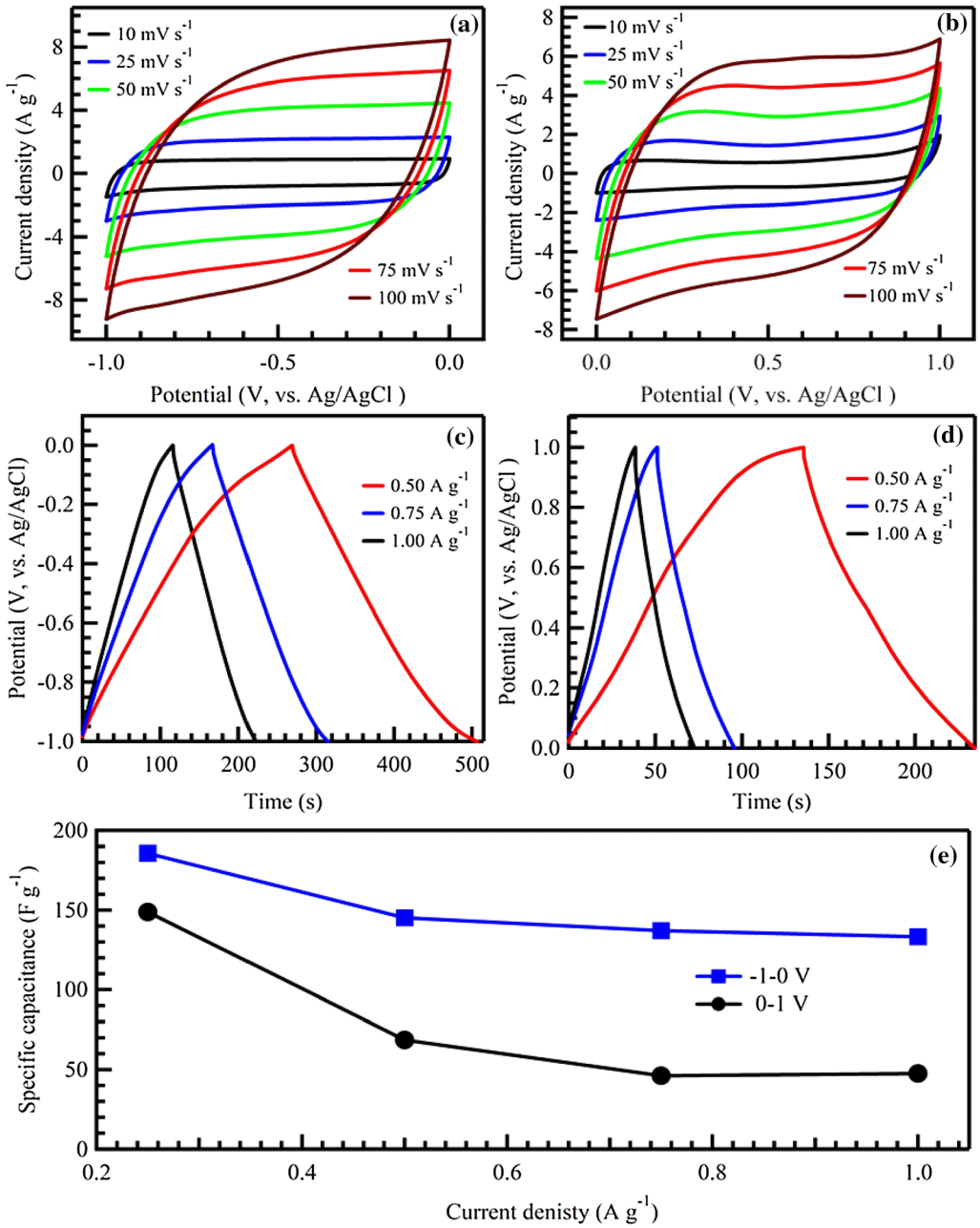

Fig. 3. Cyclic voltammograms at different scan rates under − 1–0 V (a), and 0–1 V (b), galvanostatic charge–discharge curves under different current densities under − 1–0 V (c), and 0–1 V (d), and specific capacitance dependence on current density (e) for rGONS in 1 M Na_2SO_4.

of rGONS was found to be 149 and 186 F g^{-1} at 0.25 A g^{-1} in 0–1 V and − 1–0 V, respectively. The high C_s can be attributed to the nanosheet morphology and mesoporosity, which were accessible to the electrolyte ions.

Practical Supercapacitor Performance

As discussed in the 3ES measurements, in Na_2SO_4, the electrode works in the range from − 1 V to 1 V; therefore, the full cell (device) can work up to 2 V. Figure 4(a–d) shows the CV curves in different potential ranges from 0–2 V at different scan rates for rGONS//rGONS, indicating higher potentials could be achieved and more energy could be stored.

The operating voltage window stability of rGONS//rGONS has been further investigated by the galvanostatic CDC. Figure 5(a–d) shows the CDC curves in the different potential ranges from 0 to 2 V for representative currents. Linear CDC curves with an ignored iR drop are shown, indicating the low resistance and better EDL performance of the rGONS electrode. It is recognized that the rGONS symmetric supercapacitor shows a wide range from 0 to 2 V, which is higher than the potential range tested elsewhere in 1 M Li_2SO_4.[55]

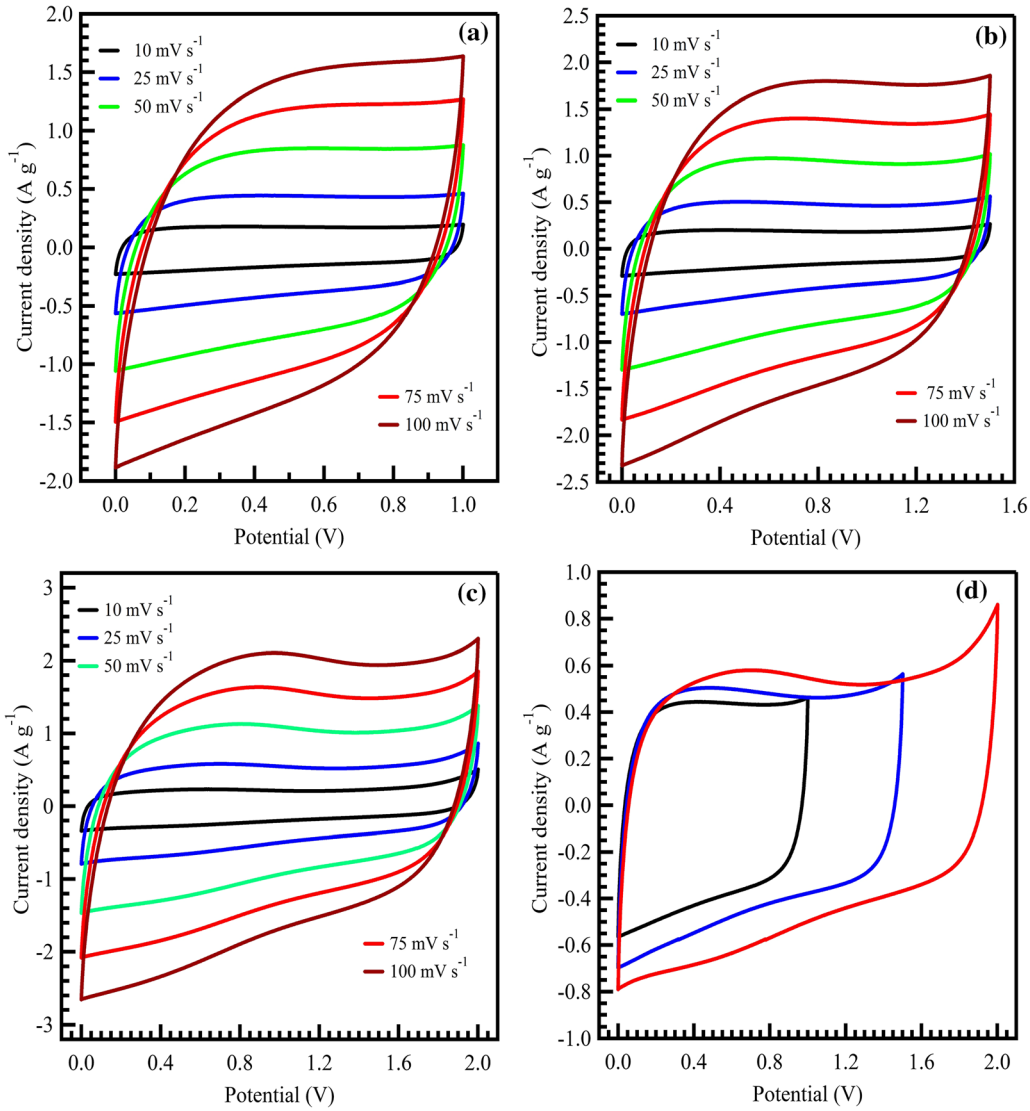

Fig. 4. Cyclic voltammograms at different scan rates under (a) 0–1 V, (b) 0–1.5 V, (c) 0–2 V and (d) 25 mV s^{-1} under different potential windows for rGONS//rGONS in 1 M Na_2SO_4.

Moreover, the C_s of rGONS//rGONS was found to be 128 F g^{-1}, 120 F g^{-1}, and 116 F g^{-1} at 0.25 A g^{-1}, as shown in Fig. 5(e) under 0–1.0 V, 0–1.5 V, and 0–2.0 V, respectively. These values are higher than those obtained by Kishore and co-workers where they obtained 80 F g^{-1} at 0.025 A g^{-1}, [56] and very close to the reported value for chemically-modified graphene in aqueous electrolytes.[32]

Figure 6(a, b) shows the CV curves at different scan rates for a MnO_2-NF//rGONS asymmetrical supercapacitor under the indicated potential windows (0–1 V and 0–2 V). The CV exhibits rectangular curves with no redox process, which reveals the ideal capacitive behaviour. Moreover, linear CDC curves at different current densities under the potential ranges are shown in Fig. 6(c, d). The C_s was found to be 177.6 F g^{-1} at 0.25 A g^{-1}, and it decreased with increasing current density, as shown in Fig. 6(e). Detailed comparison examples are shown in Fig. 6(e) and Table I. The high specific capacitance can be ascribed to the nanosheet morphology and mesoporosity for both the MnO_2 and graphene nanosheet structures which were accessible to the electrolyte ions.[57]

The Ragone plot for MnO_2-NF//rGONS is shown in Fig. 6(f), showing a high energy density of 24.7 W h kg^{-1} at a power density of 360.9 W h kg^{-1} in Na_2SO_4 (0–2) V. This high energy density indicates that more charge is stored in this supercapacitor as a result of the electroactive electrode materials and the wide potential range.[69] The energy density remained at 6.2 Wh kg^{-1} at a high power density of 2.2 kW kg^{-1}. The current findings are higher than those reported for related systems (MnO_2//Fe_3O_4, $RuO_2{\cdot}xH_2O$/carbon nano-onions, MnO_2//rGO, MnO_2//AC, MnO_2/$MnCO_3$/rGO//rGO aerogel and MnO_2/rGO//AC, which gave 8.1, 11.6, 12.5, 16.4, 18.7 and 21.0 Wh kg^{-1}, respectively [5,59,63–65,70]). On the other

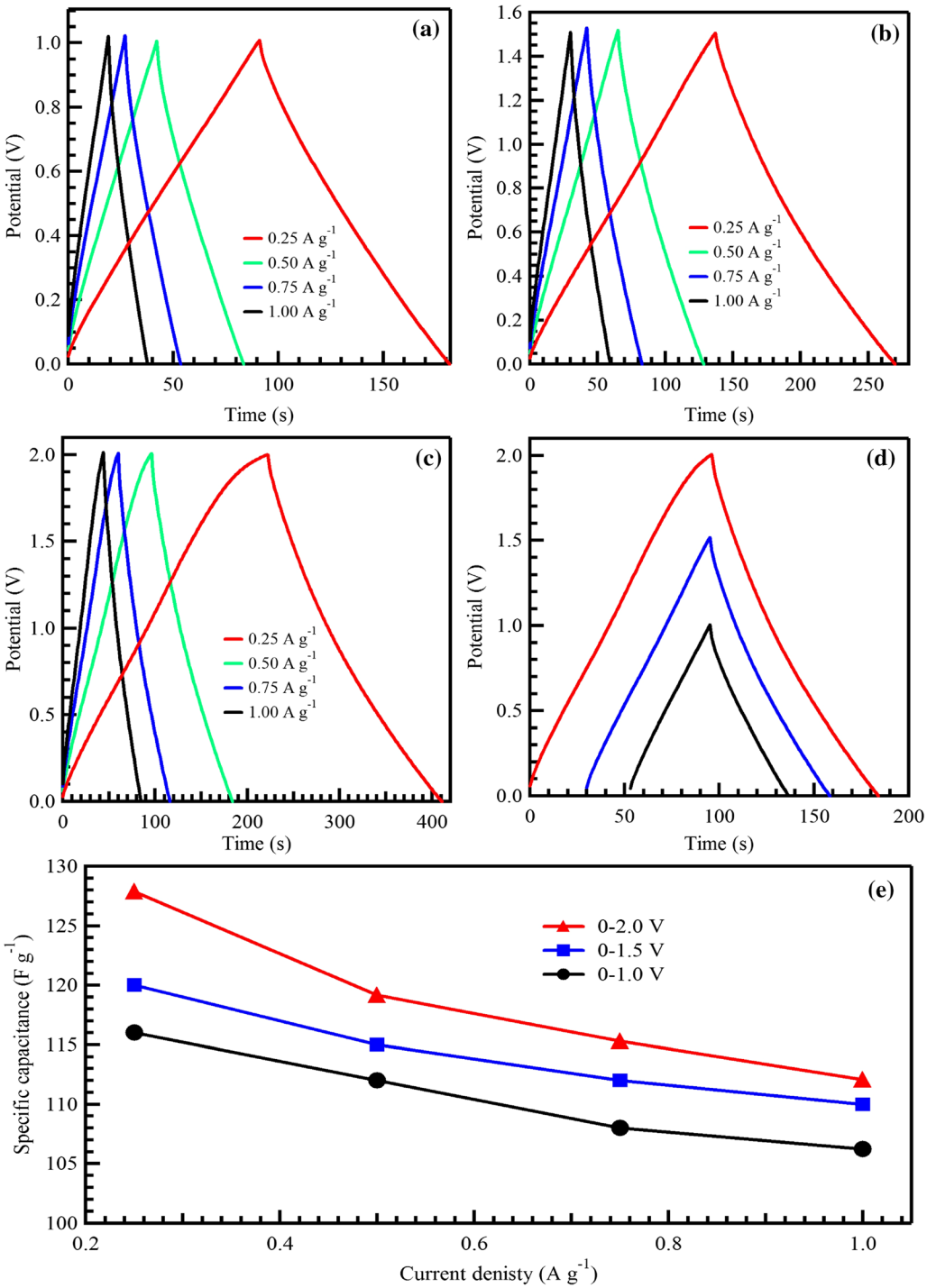

Fig. 5. Galvanostatic charge–discharge curves at different current densities under (a) 0–1 V, (b) 0–1.5 V, (c) 0–2 V, (d) 0.5 A g^{-1} under different potential windows and (e) specific capacitance dependence on current density for rGONS//rGONS in 1 M Na_2SO_4.

hand, the rGONS//rGONS symmetric supercapacitor shows a high energy density of 17.7 Wh kg^{-1}, which is higher than those reported for pure carbon materials, such as porous carbon nanoparticles (11.1 Wh kg^{-1} [60]) and SWCNT (11.4 Wh kg^{-1} [42]). A detailed comparison is given in Table I.

The long-life stability of the MnO_2-NF//rGONS supercapacitor has been tested. Figure 7 (left versus bottom), shows high cyclic stability reaching 95.2% at 1 A g^{-1} over 4000 cycles. Moreover, Fig. 7 (left versus bottom) shows the Coulombic efficiency of around 91% overall cycling range. The insets show

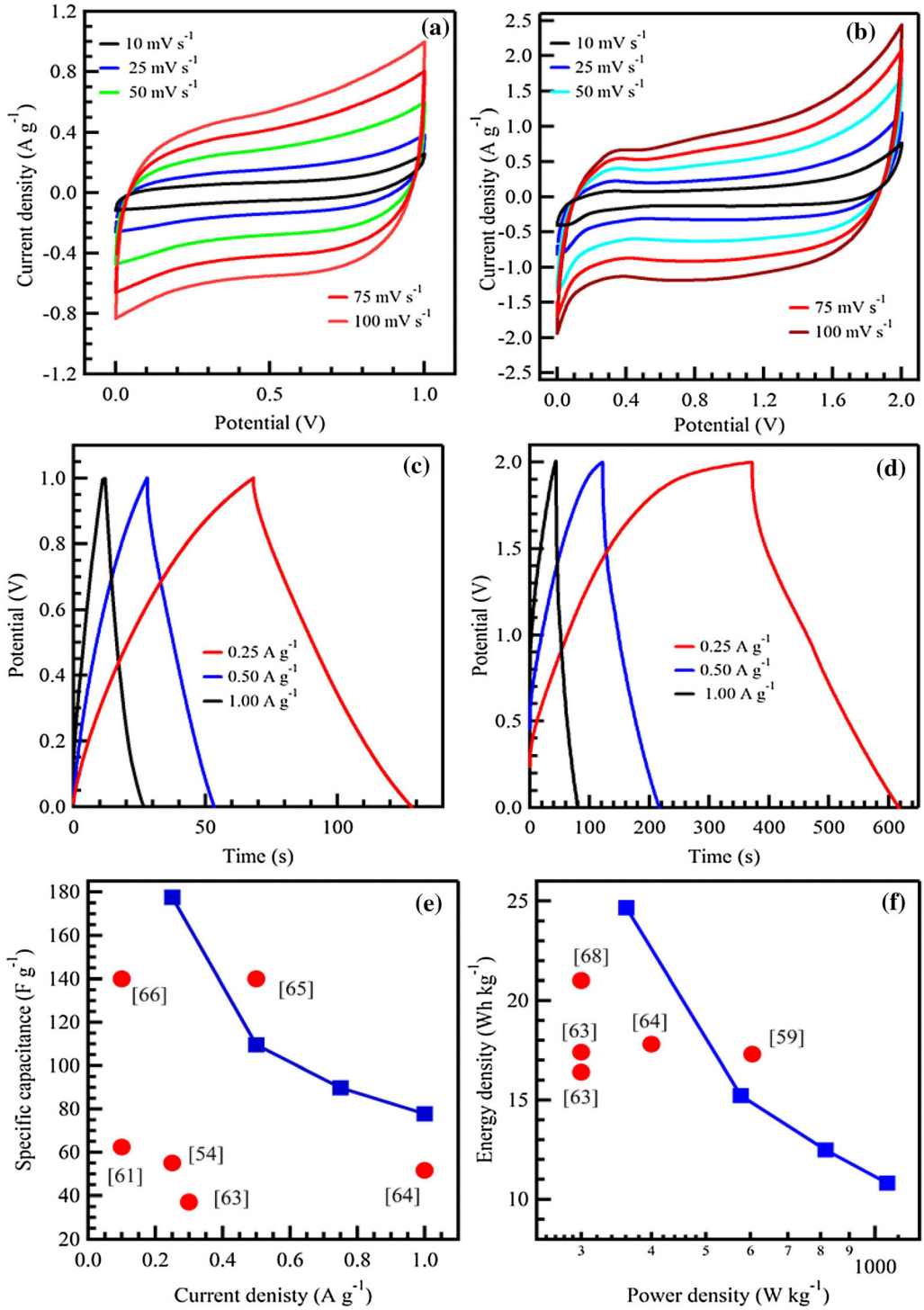

Fig. 6. Cyclic voltammograms at the different scan rates under (a) 0–1 V and (b) 0–2 V, galvanostatic charge–discharge curves under different current densities under (c) 0–1 V and (d) 0–2 V, specific capacitance dependence on current density (e) and Ragone plot (f) for MnO_2-NF// rGONS in 1 M Na_2SO_4.

the 1st–5th and 4000th CDC cycles, indicating the similarity of the test. The stability and Columbic efficiency of rGONS//rGONS (cyclic stability of 96% and Coulombic efficiency of 90% over 1000 cycles) are shown in Supplementary Fig. S2.

Furthermore, the supercapacitor stability was tested using EIS analysis, where the impedance spectra were performed before and after the 4000 CDC cycles. Supplementary Fig. S3(a, b) shows Nyquist and Bode plots for MnO_2-NF//rGONS. The

Table I. Comparison of reported specific capacitance, stability, and energy density with graphene and MnO_2-based asymmetric supercapacitors

Supercapacitors type	Supercapacitors electrode materials	Specific capacitance (F g^{-1})	Cell potential (V)	Stability (%) @ no of cycles	Energy density (Wh kg^{-1})	Electrolyte	References
Symmetric	MWCNTs-Cyst//MWCNTs-Cyst	23.0 @ 0.25 A g^{-1}	1.0	90.0 @ 11,000	–	1 M Na_2SO_4	58
Symmetric	MnO_2//MnO_2	36.0 @ 0.30 A g^{-1}	1.0	–	3.3	0.1 M K_2SO_4	59
Symmetric	Porous carbon nanoparticles//porous carbon nanoparticles	309.0 @ 0.06 A g^{-1}	1.0	95.0 @ 2500	11.1	5 M KOH	60
Symmetric	SWCNT//SWCNT	80.0 @ 1.0 A g^{-1}	2.0	–	11.4	1 M Na_2SO_4	42
Symmetric	Porous nanocarbons//porous nanocarbons	368.0 @ 0.06 A g^{-1}	1.0	96.0 @ 1700	13.0	5 M KOH	15
Symmetric	Carbon nanospheres// Carbon nanospheres	129.0 @ 0.10 A g^{-1}	1.6	94.0 @ 5200	17.9	5 M KOH	13
Symmetric	rGONS//rGONS	128.0 @ 0.25 A g^{-1}	2.0	96.0 @ 1000	17.7	1 M Na_2SO_4	This work
Asymmetric	MnO_2//AC	62.4 @ 0.10 A g^{-1}	1.5	81.4 @ 1500	–	1 M LiOH	61
Symmetric	rGONS//rGONS	140.0 @ 0.05 A g^{-1}	1.0	86.0 @ 1100	5.0	5 M KOH	40
Asymmetric	MnO_2//Fe_3O_4	21.5 @ 0.30 A g^{-1}	1.8	–	8.1	0.1 M K_2SO_4	59
Asymmetric	MnO_2/CNT//AC	–	1.5	–	13.3	1 M Na_2SO_4	62
Asymmetric	MnO_2//AC	29.0 @ 0.30 A g^{-1}	2.0	64.4 @ 5000	16.4	0.1 M $Ba(NO_3)_2$	63
Asymmetric	MnO_2//AC	31.0 @ 0.30 A g^{-1}	2.0	–	17.3	0.1 M K_2SO_4	59
Asymmetric	MnO_2//AC	37.0 @ 0.30 A g^{-1}	2.0	82.6 @ 5000	17.4	0.1 M $Mg(NO_3)_2$	63
Asymmetric	MnO_2/$MnCO_3$/rGO//rGO	51.6 @ 1.00 A g^{-1}	1.6	84.1 @ 2000	17.8	1 M Na_2SO_4	64
Asymmetric	a-MnO_2//AC	55.0 @ 0.25 A g^{-1}	2.0	93.0 @ 100	20.8	1 M KCl	54
Asymmetric	MnO_2//AC	32.0 @ 0.30 A g^{-1}	2.0	75.5 @ 5000	21.0	0.1 M $Ca(NO_3)_2$	63
Asymmetric	MnO_2/rGO//AC	140.0 @ 0.50 A g^{-1}	2.0	100.0 @ 5000	21.0	1 M Na_2SO_4	65
Asymmetric	MnO_2//AC	140.0 @ 0.10 A g^{-1}	2.0	88.0 @ 1000	21.0	2 M KNO_3	66
Asymmetric	MnO_2//rGO hydrogel	59.6 @ 1.00 A g^{-1}	1.6	89.6 @ 1000	21.2	1 M Na_2SO_4	67
Asymmetric	MnO_2-rGO//rGO	153.0 @ 0.50 A g^{-1}	2.0	56.0 @ 1000	23.6	1 M Li_2SO_4	68
Asymmetric	MnO_2-*NF*//*rGONS*	177.6 @ 0.25 A g^{-1}	2.0	95.2 @ 4000	24.7	1 M Na_2SO_4	This work

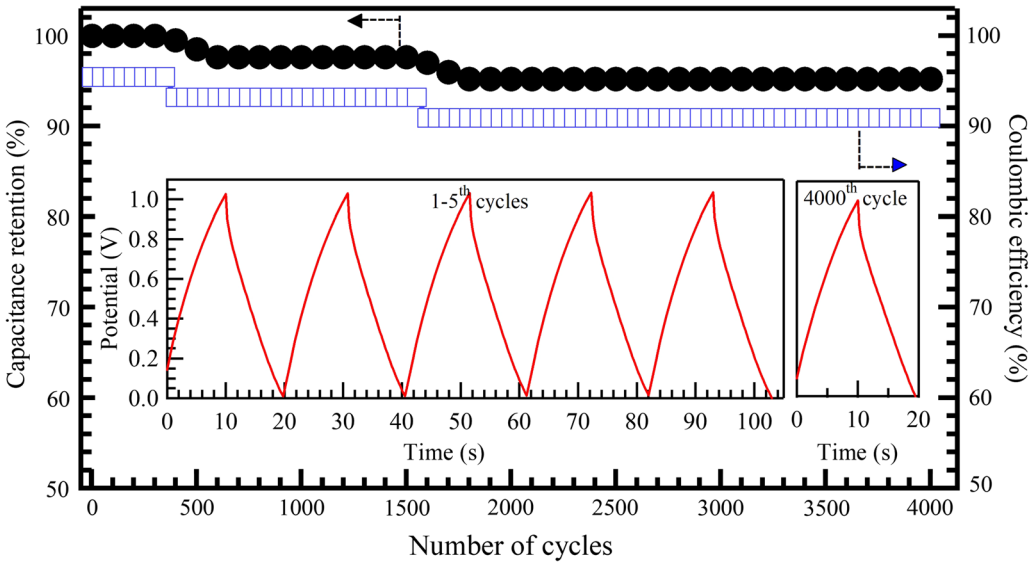

Fig. 7. Stability and Columbic efficiency curves for MnO_2-NF//rGONS in 1 M Na_2SO_4; *insets* some selected CDC cycles.

supercapacitor shows a semi-circle and then an almost straight line in the high- and low-frequency regions, respectively. From data fitting, the electrochemical parameters, including solution resistance (R_s), charge transfer resistance (R_{ct}), capacitance (C), constant phase element (CPE), Warburg (W), electrochemical surface area (S_E) and relaxation time, were obtained and are listed in Supplementary Table S1. MnO_2-NF//rGONS shows very low R_s and R_{ct} values of 1.95 and 4.51 Ω, respectively, which is lower than reported for porous NiO//porous NiO (10 Ω–20 Ω) [36] and MnO_2/$MnCO_3$/rGO//rGO (7 Ω).[64] The supercapacitor shows low resistance values, indicating its suitability for energy storage. In addition, the slight change in the parameters before and after 4000 CDC cycles confirms the supercapacitor electrochemical stability.

CONCLUSIONS

MnO_2 nanoflowers recovered from a Zn-C battery showed excellent electrochemical performance as a positive electrode. On the other hand, mesoporous reduced graphene oxide nanosheets were investigated as a negative electrode material for supercapacitor applications. The single electrodes of MnO_2 nanoflowers as an anode and rGO nanosheets as a cathode exhibit a high specific capacitance of 207 F g^{-1} and 145 F g^{-1}, respectively, at 0.5 A g^{-1}). The asymmetrical supercapacitor was fabricated from both materials and electrochemically evaluated. It shows a superb supercapacitive performance up to 2.0 V in aqueous electrolytes. The asymmetrical supercapacitor produces a high specific capacitance of 177.6 F g^{-1} and a high energy density of 24.7 Wh kg^{-1} with a high stability of 95.2% over 4000 cycles. The findings recommend a combination of MnO_2 nanoflowers and rGO nanosheets as an asymmetric supercapacitor.

ACKNOWLEDGMENT

Dr. Gomaa A.M. Ali would like to express his gratitude to Associate Prof. Kwok Feng Chong (Faculty of Industrial Sciences & Technology, Universiti Malaysia Pahang) for his help and for providing the tools during conducting the experiments.

CONFLICT OF INTEREST

The author declares that there is no conflict of interest.

ELECTRONIC SUPPLEMENTARY MATERIAL

The online version of this article (https://doi.org/10.1007/s11664-020-08268-7) contains supplementary material, which is available to authorized users.

REFERENCES

1. H. Zhang, L. Zhang, J. Chen, H. Su, F. Liu, and W. Yang, *J. Power Sour.* 315, 120 (2016).
2. H. Su, H. Huang, H. Zhang, X. Chu, B. Zhang, B. Gu, X. Zheng, S. Wu, W. He, C. Yan, J. Chen, and W. Yang, *ACS Appl. Energy Mater.* 1, 3544 (2018).
3. H. Su, H. Huang, S. Zhao, Y. Zhou, S. Xu, H. Pan, B. Gu, X. Chu, W. Deng, H. Zhang, H. Zhang, J. Chen, W. Yang, and A.C.S. Appl, *Mater. Interfaces* 12, 2773 (2020).
4. G. Zan, T. Wu, P. Hu, Y. Zhou, S. Zhao, S. Xu, J. Chen, Y. Cui, and Q. Wu, *Energy Storage Mater.* 28, 82 (2020).
5. G. Yu, L. Hu, M. Vosgueritchian, H. Wang, X. Xie, J.R. McDonough, X. Cui, Y. Cui, and Z. Bao, *Nano Lett.* 11, 2905 (2011).
6. E.A.A. Aboelazm, G.A.M. Ali, H. Algarni, H. Yin, Y.L. Zhong, and K.F. Chong, *J. Phys. Chem. C* 122, 12200 (2018).

7. G.A.M. Ali, O.A. Fouad, S.A. Makhlouf, M.M. Yusoff, and K.F. Chong, *J. Solid State Electrochem.* 18, 2505 (2014).
8. E.K. Kim, N.K. Shrestha, W. Lee, G. Cai, and S.H. Han, *Mater. Chem. Phys.* 155, 211 (2015).
9. K. Wang, H. Wu, Y. Meng, and Z. Wei, *Small* 10, 14 (2014).
10. E.A.A. Aboelazm, G.A.M. Ali, H. Algarni, and K.F. Chong, *Curr. Nanosci.* 14, 1 (2018).
11. H. Bigdeli, M. Moradi, S. Borhani, E.A. Jafari, S. Hajati, and M.A. Kiani, *Phys. E* 100, 45 (2018).
12. J. Yesuraj, E. Elanthamilan, B. Muthuraaman, S.A. Suthanthiraraj, and J.P. Merlin, *J. Electron. Mater.* 48, 7239 (2019).
13. G.A.M. Ali, A. Divyashree, S. Supriya, K.F. Chong, A.S. Ethiraj, M. Reddy, H. Algarni, and G. Hegde, *Dalton Trans.* 46, 14034 (2017).
14. C. Liu, Z. Yu, D. Neff, A. Zhamu, and B.Z. Jang, *Nano Lett.* 10, 4863 (2010).
15. G.A.M. Ali, S.A.A. Manaf, D. A, K.F. Chong, and G. Hegde, *J. Energy Chem*. 25(4), 734 (2016).
16. I. Grygorchak, R. Shvets, I.V. Kityk, A.V. Kityk, R. Wielgosz, O. Hryhorchak, and I. Shchur, *Phys. E* 108, 164 (2019).
17. J. Zhang, S. Ali, F. Liu, A. Ali, K. Wang, and X. Wang, *J. Electron. Mater.* 48, 4196 (2019).
18. W. Liu, J. Chen, Z. Chen, K. Liu, G. Zhou, Y. Sun, M.-S. Song, Z. Bao, and Y. Cui, *Adv. Energy Mater.* 7, 1701076 (2017).
19. K. Liu, B. Kong, W. Liu, Y. Sun, M.-S. Song, J. Chen, Y. Liu, D. Lin, A. Pei, and Y. Cui, *Joule* 2, 1857 (2018).
20. J. Wan, J. Xie, X. Kong, Z. Liu, K. Liu, F. Shi, A. Pei, H. Chen, W. Chen, J. Chen, X. Zhang, L. Zong, J. Wang, L.-Q. Chen, J. Qin, and Y. Cui, *Nat. Nanotechnol.* 14, 705 (2019).
21. S.-M. Xu, X. Liang, X.-Y. Wu, S.-L. Zhao, J. Chen, K.-X. Wang, and J.-S. Chen, *Nat. Commun.* 10, 5810 (2019).
22. H. Jang, S. Suzuki, and M. Miyayama, *J. Electrochem. Soc.* 159, 1425 (2012).
23. H. Wei, J. Wang, S. Yang, Y. Zhang, T. Li, and S. Zhao, *Phys. E* 83, 41 (2016).
24. S.L. Chou, F.Y. Cheng, and J. Chen, *J. Power Sour.* 162, 727 (2006).
25. T. Yousefi, A.N. Golikand, M. Hossein Mashhadizadeh, and M. Aghazadeh, *J. Solid State Chem.* 190, 202 (2012).
26. T. Yousefi, R. Davarkhah, A.N. Golikand, and M.H. Mashhadizadeh, *Mater. Sci. Semicond. Process.* 16, 868 (2013).
27. G. Yang, B. Wang, W. Guo, Z. Bu, C. Miao, T. Xue, and H. Li, *Mater. Res. Bull.* 47, 3120 (2012).
28. M. Dong, Y.X. Zhang, H.F. Song, X. Qiu, X.D. Hao, C.P. Liu, Y. Yuan, X.L. Li, and J.M. Huang, *Phys. E* 45, 103 (2012).
29. D. Yan, Z. Guo, G. Zhu, Z. Yu, H. Xu, and A. Yu, *J. Power Sour.* 199, 409 (2012).
30. G.A.M. Ali, M.M. Yusoff, E.R. Shaaban, and K.F. Chong, *Ceram. Int.* 43, 8440 (2017).
31. G.A.M. Ali, L.L. Tan, R. Jose, M.M. Yusoff, and K.F. Chong, *Mater. Res. Bull.* 60, 5 (2014).
32. M.D. Stoller, S. Park, Y. Zhu, J. An, and R.S. Ruoff, *Nano Lett.* 8, 3498 (2008).
33. P.E. Marina, G.A.M. Ali, L.M. See, E.Y.L. Teo, E.-P. Ng, and K.F. Chong, *Arabian J. Chem*. 12, 3883 (2019).
34. G.A.M. Ali, M.R. Thalji, W.C. Soh, H. Algarni, and K.F. Chong, *J. Solid State Electrochem.* 24, 25 (2020).
35. G.A.M. Ali, M.M. Yusoff, H. Algarni, and K.F. Chong, *Ceram. Int.* 44, 7799 (2018).
36. V. Ganesh, S. Pitchumani, and V. Lakshminarayanan, *J. Power Sour.* 158, 1523 (2006).
37. J. Yin and J. Park, *J. Solid State Electrochem.* 19, 2391 (2015).
38. A.S. Adekunle, K.I. Ozoemena, B.B. Mamba, B.O. Agboola, and O.S. Oluwatobi, *Int. J. Electrochem. Sci.* 6, 4760 (2011).
39. W.S. Hummers and R.E. Offeman, *J. Am. Chem. Soc.* 80, 1339 (1958).
40. G.A.M. Ali, S.A. Makhlouf, M.M. Yusoff, and K.F. Chong, *Rev. Adv. Mater. Sci.* 40, 35 (2015).
41. A. Bello, O.O. Fashedemi, M. Fabiane, J.N. Lekitima, K.I. Ozoemena, and N. Manyala, *Electrochim. Acta* 114, 48 (2013).
42. P.-C. Chen, G. Shen, Y. Shi, H. Chen, and C. Zhou, *ACS Nano* 4, 4403 (2010).
43. E.A.A. Aboelazm, G.A.M. Ali, and K.F. Chong, *Chem. Adv. Mater.* 3, 67 (2018).
44. Z. Bo, Z. Wen, H. Kim, G. Lu, K. Yu, and J. Chen, *Carbon* 50, 4379 (2012).
45. L. Demarconnay, E. Raymundo-Piñero, and F. Béguin, *Electrochem. Commun.* 12, 1275 (2010).
46. T.H. Lee, D.T. Pham, R. Sahoo, J. Seok, T.H.T. Luu, and Y.H. Lee, *Energy Storage Mater.* 12, 223 (2018).
47. G.A.M. Ali, O.A. Habeeb, H. Algarni, and K.F. Chong, *J. Mater. Sci.* 54, 683 (2019).
48. S. Trasatti and O. Petrii, *Pure Appl. Chem.* 63, 711 (1991).
49. S. Trasatti and O. Petrii, *J. Electroanal. Chem.* 327, 353 (1992).
50. J. Gamby, P.L. Taberna, P. Simon, J.F. Fauvarque, and M. Chesneau, *J. Power Sour.* 101, 109 (2001).
51. G.A.M. Ali, O.A.G. Wahba, A.M. Hassan, O.A. Fouad, and K.F. Chong, *Ceram. Int.* 41, 8230 (2015).
52. D.P. Dubal, D.S. Dhawale, T.P. Gujar, and C.D. Lokhande, *Appl. Surf. Sci.* 257, 3378 (2011).
53. P. Yu, X. Zhang, Y. Chen, and Y. Ma, *Mater. Lett.* 64, 1480 (2010).
54. M.S. Hong, S.H. Lee, and S.W. Kim, *Electrochem. Solid-State Lett.* 5, A227 (2002).
55. X. Yang, Y.S. He, G. Jiang, X.Z. Liao, and Z.F. Ma, *Electrochem. Commun.* 13, 1166 (2011).
56. M.S. Kishore, P. Srimathi, S. Kumar, S. Addepalli, S. Swaminathan, V. Tilak, and R. Colborn, *Bull. Mater. Sci.* 36, 667 (2013).
57. Y. Qian, S. Lu, and F. Gao, *J. Mater. Sci.* 46, 3517 (2011).
58. G.A.M. Ali, E.Y. Lih Teo, E.A.A. Aboelazm, H. Sadegh, A.O.H. Memar, R. Shahryari-Ghoshekandi, and K.F. Chong, Mater. *Chem. Phys.* 197, 100 (2017).
59. T. Cottineau, M. Toupin, T. Delahaye, T. Brousse, and D. Bélanger, *Appl. Phys. A* 82, 599 (2006).
60. G.A.M. Ali, S.A. Abdul Manaf, A. Kumar, K.F. Chong, and G. Hegde, *J. Phys. D* 47, 495307 (2014).
61. A. Yuan and Q. Zhang, *Electrochem. Commun.* 8, 1173 (2006).
62. L. Li, Z.A. Hu, N. An, Y.Y. Yang, Z.M. Li, and H.Y. Wu, *J. Phys. Chem. C* 118, 22865 (2014).
63. C. Xu, H. Du, B. Li, F. Kang, and Y. Zeng, *J. Electrochem. Soc.* 156, A435 (2009).
64. Y. Liu, D. He, H. Wu, J. Duan, and Y. Zhang, *Electrochim. Acta* 164, 154 (2015).
65. E. Miniach, A. Śliwak, A. Moyseowicz, L. Fernández-Garcia, Z. González, M. Granda, R. Menendez, and G. Gryglewicz, *Electrochim. Acta* 240, 53 (2017).
66. V. Khomenko, E. Raymundo-Piñero, and F. Béguin, *J. Power Sour.* 153, 183 (2006).
67. S. Wu, W. Chen, and L. Yan, *J. Phys. Chem. A* 2, 2765 (2014).
68. C.J. Jafta, F. Nkosi, L. le Roux, M.K. Mathe, M. Kebede, K. Makgopa, Y. Song, D. Tong, M. Oyama, N. Manyala, S. Chen, and K.I. Ozoemena, *Electrochim. Acta* 110, 228 (2013).
69. Z.J. Fan, J. Yan, T. Wei, L.J. Zhi, G.Q. Ning, T.Y. Li, and F. Wei, *Adv. Funct. Mater.* 21, 2366 (2011).
70. R. Borgohain, J. Li, J.P. Selegue, and Y.T. Cheng, *J. Phys. Chem. C* 116, 15068 (2012).